RSC Advances

PAPER

View Article Online
View Journal | View Issue

Cite this: *RSC Adv.*, 2018, **8**, 35551

Effect of metal–ligand ratio on the CO_2 adsorption properties of Cu–BTC metal–organic frameworks†

Yuanyuan Liu, [a] Suqin Liu, [b] Alexandre A. S. Gonçalves [a] and Mietek Jaroniec *[a]

Received 19th September 2018
Accepted 10th October 2018

DOI: 10.1039/c8ra07774f

rsc.li/rsc-advances

Initially, in the synthesis of Cu–BTC MOFs some fraction of Cu was expected to be replaced with Mg to enhance its CO_2 adsorption properties. Indeed, an enhancement in the specific surface area, microporosity and CO_2 adsorption capacity was observed; however, Mg was not detected. Therefore, additional syntheses of Cu–BTC MOFs with the same Cu to BTC ratios were performed but in the absence of Mg to explain the observed enhancement. It was found that the adjustment of the Cu–BTC ratio to 1.09 : 1.0, which differs from that reported in the literature, resulted in a Cu–BTC MOF with higher specific BET surface area, larger micropore volume, and consequently, superior CO_2 adsorption of 9.33 mmol g^{-1} at 0 °C and 1 bar.

Introduction

Carbon dioxide (CO_2) is one of the most significant greenhouse gases. The increasing CO_2 concentration in the atmosphere is one of the major factors causing global warming. In fact, the atmosphere CO_2 concentration was reported to continuously increase every year because of the continuous consumption of fossil fuels.[1] Therefore, the decrease of CO_2 concentration in the atmosphere is urgently needed for the sustainable development of our world. Recently, CO_2 sequestration has emerged as one of the most promising technologies to defer global warming.[2] As a result, various novel strategies for CO_2 capture and storage have been reported, including membrane separation,[3] adsorption,[4] and cryogenic distillation.[5] In particular, solid adsorbents have been widely studied for CO_2 sequestration because of their environmental friendliness and low energy consumption.[6] Although numerous porous solids have been developed for physical adsorption of CO_2, many issues should be solved before their commercialization. Among them, the controlled synthesis of adsorbents with desirable structural properties is of great importance for efficient adsorption of CO_2.

Recently, metal–organic frameworks (MOFs) have gained an increasing attention for gas separations and adsorption owing to their tailorable chemical structures and versatile structural properties.[7,8] MOFs are microporous crystalline materials formed *via* coordination chemistry between metal ions/clusters and organic spacers into a three dimensional periodic network.[9] Their pore size, surface area and ligand functionalities can be easily tuned *via* selection of suitable metals clusters and organic linkers,[10] as well as through the post-synthetic modification.[11] MOFs are desirable for gas adsorption and separation because of their ultrahigh micropore volume and large specific surface area.[12] More than several thousands of different MOFs have been reported so far,[13] in which Cu–BTC is one of the most widely studied framework. Cu–BTC, also known as HKUST-1, was first reported by Chui *et al.* in Science in 1999,[14] and this MOF and its derivatives were widely studied for gas adsorption.[15] The well-established Cu–BTC framework can be simply assembled between copper cation and benzene-1,3,5-tricarboxylate (BTC) ligand into a microporous face centred-cubic crystal network. As the efficient CO_2 adsorbent, Cu–BTC can adsorb CO_2 from 2.5 to 4.2 mmol g^{-1} at 25 °C and 1 bar.[16,17] In a general synthesis, Cu–BTC can be readily obtained by mixing copper nitrate and BTC ligand in a ratio of 1.81 : 1.0. To improve the CO_2 adsorption capacity of MOFs, a wide range of strategies have been reported, such as ligands modification,[18] ion-doping,[19] solvent activation,[20] formation of composites,[21,22] and optimization of the synthetic method.[17] The successful strategies can be divided into two categories: (1) involving the incorporation of chemical active sites into MOFs, and (2) enhancing both the specific area and micropore volume of these frameworks. It is of great interest to explore alternative approaches to increasethe CO_2 adsorption capacity of MOFs.

In this work, we report the effect of metal–ligand ratio on the assembly of Cu–BTC, to obtain materials with significantly higher CO_2 adsorption capacity. To enhance adsorption properties of Cu–BTC for CO_2, our intention was to incorporate the basic sites such as Mg^{2+} into this framework. However, our study found that Mg species are not present in the final Cu–BTC framework. A detailed analysis of synthesis conditions led to the

[a]*Department of Chemistry and Biochemistry, Kent State University, Kent, Ohio 44240, USA. E-mail: jaroniec@kent.edu*

[b]*School of Food Science and Technology & School of Chemical Engineering, Hubei University of Arts and Science, Xiangyang 441053, China*

† Electronic supplementary information (ESI) available: Three tables and nine figures. See DOI: 10.1039/c8ra07774f

conclusion that the adsorption properties of Cu–BTC can be well tuned by varying the metal–ligand ratio. A great improvement in the specific surface area, microporosity and CO_2 adsorption capacity was achieved by optimizing this ratio.

Results and discussion

Synthesis and characterization of Cu–BTC with Mg doping

In this study Cu–BTC MOF was prepared with a metal–ligand ratio of 1.81 : 1.0 in a mixture of ethanol/water (1 : 1) as a reference sample.[23] Through incorporation of the alkaline metal Mg species, porous solids such as mesoporous silica show high affinity to acidic CO_2 molecules, resulting in the increase of CO_2 uptake.[24] Additionally, Mg-MOF-74 is well known for the high CO_2 uptake (8.6 mmol g^{-1} at 25 °C and 1 bar) and selectivity,[25] which is attributed to the open Mg center in the MOF structure.[26,27] For attempted incorporation of Mg into Cu–BTC MOF, the total molar ratio of metals (Mg and Cu) to the BTC ligand remained constant as 1.81 : 1.0, in which the molar ratio of Mg was designed to be 20%, 40% and 60% of the total amount of both metal ions. Using the same method as that for the fabrication of pure Cu–BTC framework, the attempted incorporation of Mg into Cu–BTC was carried out by varying the amount of Mg salt during the synthesis. The resulting samples of MOF were characterized by powder X-ray diffraction (XRD), scanning electron microscopy (SEM), thermogravimetric analysis (TGA) and nitrogen adsorption (see ESI, Fig. S1–S4†). The corresponding textural properties of these three Cu–BTC frameworks are summarized in Table S1.† The enhancement in the CO_2 uptake is observed with increasing amount of the Mg salt present during synthesis (see Fig. S5 and Table S2†). Particularly, Cu–BTC prepared with addition of 40% of Mg exhibited the highest CO_2 adsorption amount of 9.31 and 5.15 mmol g^{-1} at 0 °C and 25 °C (1 bar), respectively. The CO_2 adsorption capacity of Cu–BTC with 40% of Mg (9.31 mmol g^{-1} at 0 °C and 1 bar) is significantly high among various Cu–BTC derivatives reported so far (see Table 2).

Like in the case of incorporation of alkaline metals into porous solids, we expected that Cu–BTC obtained with the addition of Mg salt would provide MOF with Mg species. To determine the role of Mg salt in the synthesis of Cu–BTC, we performed the energy-dispersive X-ray spectroscopy (EDS) analysis (see Fig. S6†). Unexpectedly, the presence of Mg element was not evidenced by EDS analysis of all three Mg (20%/40%/60%)-Cu–BTC samples. In addition, the absence of Mg in all three samples was also confirmed by atomic absorption spectroscopy analysis (data not shown). These data indicate that Mg is not involved in the formation of Cu–BTC framework, and is possibly washed out at the end of synthesis. Therefore, the observed improvements in the specific surface area, microporosity and CO_2 adsorption of the Cu–BTC samples synthesized with Mg salt are not caused by incorporation of Mg into this framework.

Since Mg was not detected in the Cu–BTC MOFs assembled in the presence of Mg salt, its addition during synthesis of Cu–BTC is indeed equivalent with changing the molar ratio between copper and BTC spacer. Therefore, we presume that the metal–ligand ratio might be the leading cause for the observed enhancement of the structural and adsorption properties.

Synthesis and characterization of Cu–BTC without Mg doping

To explain the aforementioned enhancement of the Cu–BTC samples obtained with Mg salt, we prepared the Cu–BTC samples without Mg, but by varying the molar ratio of Cu to BTC to assure the same composition as these samples obtained with Mg at the constant number of moles of both metals. Thus, pure Cu–BTC MOFs with different molar ratios of Cu to BTC were optimized, namely 1.45 : 1.0, 1.09 : 1.0 and 0.72 : 1.0, without the addition of Mg salt, to achieve the same molar ratios of Cu to BTC as in the Cu–BTC samples prepared with the addition of Mg.

The powder XRD patterns of Cu–BTC frameworks with controlled ratios of Cu to BTC are the same as that of the reference Cu–BTC (1.81 : 1.0 molar ratio of Cu to BTC; see Fig. 1). These XRD data are consistent with those on the patterns obtained for the Cu–BTC samples with attempted incorporation of Mg (see Fig. S1†) and for the reported Cu–BTC.[28] The new Cu–BTC samples show octahedral morphology, indicating that the variation of the metal–ligand ratio did not alter the sample morphology. The surface morphology of these Cu–BTC materials was examined by SEM imaging (see Fig. 2 and S2†) to show octahedral morphology (~10 to 20 μm in width). These SEM images provide further evidence about good crystallinity of the MOF studied. The SEM images in Fig. 2 show that

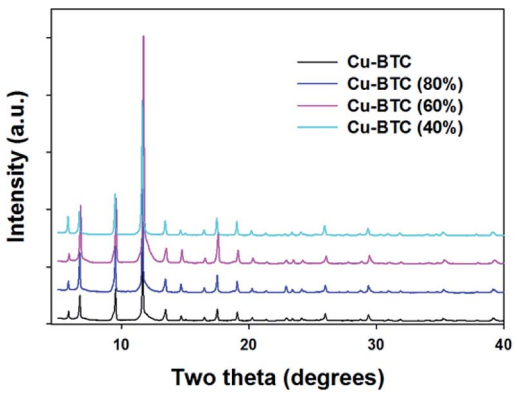

Fig. 1 The powder XRD patterns of the Cu–BTC, Cu–BTC (80%), Cu–BTC (60%), and Cu–BTC (40%) samples.

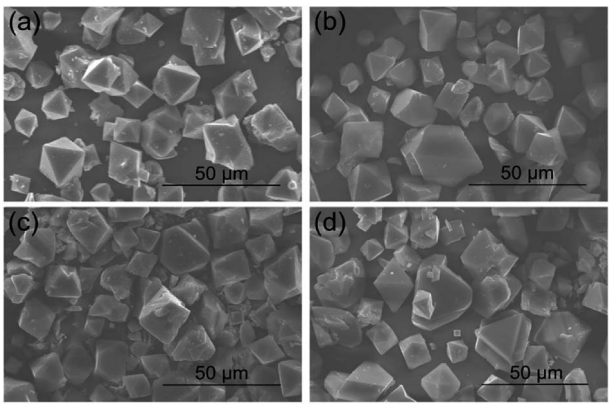

Fig. 2 SEM images of (a) Cu–BTC, (b) Cu–BTC (80%), (c) Cu–BTC (60%), and (d) Cu–BTC (40%) samples.

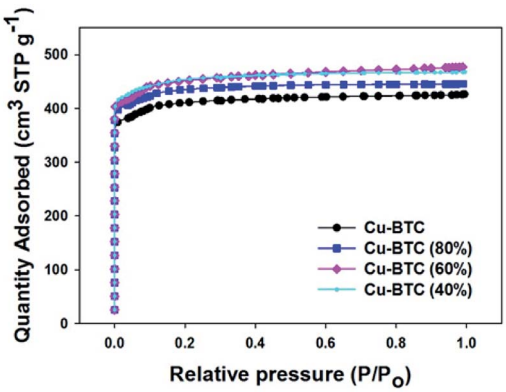

Fig. 3 Nitrogen sorption isotherms for Cu–BTC, Cu–BTC (80%), Cu–BTC (60%), and Cu–BTC (40%) samples at −196 °C.

the crystal size of Cu–BTC (80%) is smaller than that of the parent MOF, and the Cu–BTC (40%) sample has the smallest crystals among the samples studied. Meanwhile, the crystal size of Cu–BTC (60%) is larger than that of the parent MOF.

The thermal stability of these samples was analyzed by TGA. As can be seen in Fig. S7,† the TGA profiles of the samples studied are analogous. Thus, these samples show similar thermal stability as the parent MOF. The initial weight loss at ~65 °C is due to the physically adsorbed molecules (moisture and solvent molecules) inside pores. Then a plateau in the range between ~150 °C to ~250 °C indicates that the structure is stable in this temperature range. However, a sharp decrease in the weight seen at ~300 °C indicates the decomposition of the sample. In addition, the mass loss for all these samples from 250 °C to 800 °C is high, which is ~45.10%, 50.91%, 56.82% and 56.13% for the samples of Cu–BTC, Cu–BTC (80%), Cu–BTC (60%), and Cu–BTC (40%), respectively.

The specific surface area and porosity of these Cu–BTC samples were determined based on the nitrogen adsorption isotherms at −196 °C (see Fig. 3). The reversible type I adsorption isotherms indicate microporous nature of these samples. The corresponding textural properties, including BET surface area and micropore volume are summarized in Table 1. The BET surface areas of these Cu–BTC (80%/60%/40%) samples are higher than that of the parent Cu–BTC. Clearly, the BET surface area increases initially with reducing the amount of copper in the synthesis mixture. Interestingly, Cu–BTC (60%) shows high BET surface area of 1560 $m^2 g^{-1}$, which is ~10% higher than that of the pure Cu–BTC. Also, the surface area is slightly higher for Cu–BTC (40%) (1572 $m^2 g^{-1}$). Moreover, both the total and micropore volumes of these samples increase initially with reduction of the copper amount, but then almost reach a plateau. Specifically, with addition of 60% of copper salt, the total volume and micropore volume for this sample are higher by 12% and 15% as compared to the reference sample. Pore size distributions for all Cu–BTC samples exhibit two peaks, which are shown in Fig. 4. When the ratio between metal and ligand decreases, the pocket size became smaller as compared to that of the parent MOF. Cu–BTC (80%) and Cu–BTC (40%) show similar side pocket sizes (smaller than that of the parent Cu–BTC), but slightly larger than that of Cu–BTC (60%). Especially, Cu–BTC (60%) is shown to have the side pockets (~0.55 nm) and the main channel (~0.82 nm). Theoretically, the Cu–BTC network has the square-type 0.90 nm channels and the tetrahedral side pockets of 0.50 nm.[31] Therefore, the structure of Cu–BTC (60%) closely agrees with that described in the theoretical model.

CO_2 adsorption properties of Cu–BTC

As seen in Table 1, interestingly, all the properties including the BET surface area, micropore volume and CO_2 adsorption for pure Cu–BTC (80%/60%/40%) samples obtained by varying the amount of BTC match the properties of the Cu–BTC samples prepared with addition of Mg salt (Tables S1 and S2†). The Cu–BTC sample with the metal–ligand ratio of 1.09 : 1.0 shows a high specific BET surface area of 1560 $m^2 g^{-1}$ and a large micropore volume of 0.70 $cm^3 g^{-1}$. These structural properties are very close to those of Cu–BTC prepared with Mg salt (40%). In addition, the CO_2 capture amount at 0 °C and 1 bar is also similar to that of Cu–BTC fabricated with 40% of Mg salt. Through simple control of the metal–ligand ratio rather than the addition of Mg salt, we can also tune the specific BET surface area, micropore volume and CO_2 adsorption capacity. Therefore, we conclude that the ratio of Cu to BTC is essential for controlling the structural and adsorption properties of MOFs.

The CO_2 adsorption performance of all four materials was evaluated at both 0 °C (see Fig. 5a) and 25 °C (see Fig. 5b). The

Table 1 The corresponding textural properties of the Cu–BTC, Cu–BTC (80%), Cu–BTC (60%), and Cu–BTC (40%) samples and the CO_2 adsorption amount at 1 bar[a]

Samples	S_{BET} ($m^2 g^{-1}$)	V_{total} ($cm^3 g^{-1}$)	V_{micro} ($cm^3 g^{-1}$)	CO_2 uptake (mmol g^{-1})		Cu/BTC ratio
				0 °C	25 °C	
Cu–BTC	1415	0.66	0.61	8.59	4.74	1.81
Cu–BTC (80%)	1506	0.69	0.67	9.06	5.05	1.45
Cu–BTC (60%)	1560	0.74	0.70	9.33	5.15	1.09
Cu–BTC (40%)	1572	0.72	0.70	9.07	5.08	0.72

[a] S_{BET}: specific surface area was calculated by BET equation in the range of $P/P_0 = 0.05$–0.2; V_{total}: total pore volume was calculated based on the nitrogen adsorption amount at $P/P_0 = 0.99$; V_{micro}: micropore volume was calculated from the cumulative pore volume curve obtained by the 2D-NLDFT method up to pore width of 2 nm.[29,30]

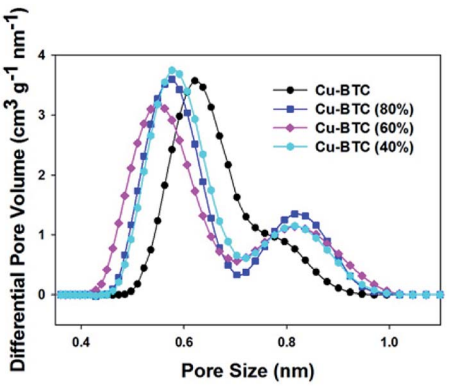

Fig. 4 Pore sizes distributions for Cu–BTC, Cu–BTC (80%), Cu–BTC (60%), and Cu–BTC (40%) samples.

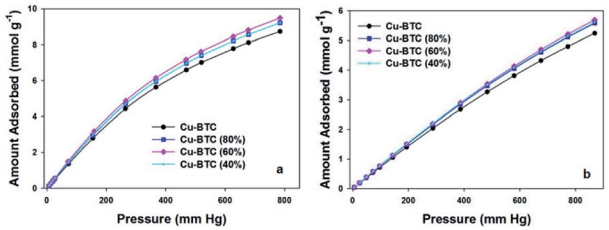

Fig. 5 CO_2 adsorption isotherms at 0 °C (a) and 25 °C (b) measured on the Cu–BTC, Cu–BTC (80%), Cu–BTC (60%), and Cu–BTC (40%) samples.

corresponding CO_2 adsorption at 1 bar of these MOFs are listed in Table 1. At either 0 °C or 25 °C, the CO_2 adsorption shows a similar trend as the changes observed for the BET surface area and microporosity. Clearly, the specific surface area and the micropore volume of these MOFs adsorbents play crucial role in the adsorption of CO_2.[4] The initial enhancement of the CO_2 uptake with decreasing amount of copper reaches a maximum and next this uptake is reduced with further decrease of Cu. Particularly, Cu–BTC (60%) exhibits the highest CO_2 uptakes of 9.33 mmol g^{-1} and 5.15 mmol g^{-1} under 1 bar at 0 °C and 25 °C, respectively. As expected, an increase in the CO_2 adsorption amount with increasing pressure is also achieved (Fig. 5). We presume that the side pockets are occupied first, and the unoccupied positions around unsaturated Cu atoms and square channels are subsequently filled with increasing pressure.[31] The presence of small micropores (<0.7 nm) was reported to be crucial for high CO_2 uptake at ambient pressures.[32] The size of side pockets is in the same range, which determines the sequence of the CO_2 uptakes at 1 bar. Having the smallest pocket size (~0.55 nm), Cu–BTC (60%) captures the highest amount of CO_2 into micropores at ambient pressure. To the best of our knowledge, the CO_2 adsorption capacity of Cu–BTC (60%) (9.33 mmol g^{-1} at 0 °C and 1 bar) is at the top CO_2 uptakes among various Cu–BTC derivatives reported so far at ambient conditions (see Table 2). In addition, the CO_2/N_2 selectivity was checked for both Cu–BTC and Cu–BTC (60%). The CO_2 and N_2 adsorption isotherms measured at 0 °C and ambient pressure are displayed in Fig. S8.† As shown in Table S3,† Cu–BTC (60%) shows higher selectivity (26.4) than the parent MOF. Recyclability is another important issue for solid adsorbents. The relevant data for Cu–BTC (60%) are shown in Fig. S9,† illustrating a good reusability of this sorbent over four adsorption–desorption cycles.

Currently, the porosity engineering to tune adsorption properties of MOFs is of great interest and achievable by direct synthesis and/or post-modification processes. These approaches likely create defects in the form of missing organic linkers and/or metal sites in the MOF structures.[38–42] For example, organic ligand defects can increase the surface areas and porosity of MOFs.[43] In fact, the presence of defects in MOFs is difficult to be quantitatively evaluated.[39] Since the molar ratio between copper and BTC spacer was intentionally tuned, an increase in the BTC linker percentage in the synthesis mixture likely resulted in the structural defects. Therefore, the smaller Cu/BTC ratio (1.09 : 1.0) in the synthesis of Cu–BTC likely generated more defects, which resulted in the enhancement of porosity and adsorption properties of this sample in comparison to the parent MOF obtained with 1.81 : 1.0 ratio.

Conclusions

In summary, we report the significance of the metal–ligand ratio in the synthesis of Cu–BTC MOFs, which can be used to tune the textural and adsorption properties of this MOF as evidenced by CO_2 adsorption studies. The Cu–BTC sample obtained with a 1.09 : 1.0 metal–ligand ratio showed the highest specific BET surface area of 1560 m^2 g^{-1}, large micropore volume of 0.70 cm^3 g^{-1} and smaller micropores (0.55 nm) among the samples studied, and consequently, the highest CO_2

Table 2 Comparison of the CO_2 adsorption uptakes at 1 bar for various Cu–BTC MOFs reported in literature

Solvents	S_{BET} (m^2 g^{-1})	V_{total} (cm^3 g^{-1})	CO_2 uptake (mmol g^{-1})	T (°C)	Ref.
H_2O/ethanol	1382	0.57	6.49	0	33
DMF	1922	0.80	7.23	0	34
DMF	1611	0.76	3.35	25	35
H_2O/ethanol/DMF	892	0.43	2.32	25	4
H_2O/ethanol	1466	0.60	4.16	25	36
H2O/ethanol	1542	0.65	2.50	27	37
H_2O/ethanol	1560	0.74	9.33	0	This work
H_2O/ethanol	1560	0.74	5.15	25	This work

adsorption of 9.33 mmol g^{-1} at 0 °C and 1 bar. In addition, Cu–BTC (60%) exhibited high CO_2/N_2 selectivity and good recyclability. We anticipated that these finding could be used for further optimization of the synthesis conditions of already reported MOFs. It is possible that their textural and adsorption properties can be further improved by controlling the metal–ligand ratio and other experimental conditions. Further studies of defects engineering in MOFs are in progress.

Experimental section

General materials

All chemicals used in this work are commercially available: copper nitrate trihydrate (99%, Acros Organics), magnesium nitrate hexahydrate (99%, Sigma-Aldrich), 1,3,5-tricarboxybenzene (95%, Strem Chemicals), ethanol (91%, Pharmco). These chemicals were directly utilized in all experiments without any further purification. Deionized water from the Milli-Q water purification system was used in all experiments.

Synthesis of Cu–BTC MOF

Cu–BTC samples were prepared using a slightly modified method reported elsewhere.[23] A copper solution obtained by dissolving $Cu(NO_3)_2 \cdot 3H_2O$ (0.875 g) in water (12 mL) was added into a solution of 1,3,5-tricarboxybenzene (H_3BTC, 0.42 g) dissolved in ethanol (12 mL) at room temperature. The metal–ligand molar ratio in this reaction was 1.81 : 1.0. After stirring for 20 min at room temperature, the mixture was transferred into an autoclave, and was kept at 120 °C for another 12 h. A blue powder product was obtained after centrifugation. The obtained powder was dried at 120 °C under vacuum for 20 h.

The synthesis of Cu–BTC MOFs carried out in the presence of Mg salt was similar to that provided above for the preparation of Cu–BTC. However, the molar ratio of both metals (Mg and Cu) to BTC ligand was kept the same (1.81 : 1.0) for a series of samples obtained by using 20%, 40% and 60% of Mg in the total number of moles of both metal components. Copper nitrate trihydrate and magnesium nitrate hexahydrate were dissolved in water (12 mL), and 1,3,5-tricarboxybenzene was dissolved in ethanol (12 mL). The aqueous solution mixture was added to the ethanol solution and stirred for 20 minutes. Then the resulting reaction mixture was transferred to autoclave, and kept in oven at 120 °C for 12 h. Finally, a blue powder product was centrifuged from the reaction mixture and further dried at 120 °C under vacuum for 20 hours. When the molar ratio of Mg was 20%, 40% and 60% of the total number of moles of both metal components, the product was labeled as Mg *X*%-Cu–BTC where $X = 20$, 40 or 60.

Another series of Cu–BTC was synthesized without Mg salt by using only 80%, 60% and 40% of Cu salt but keeping the same amount of H_3BTC. Varying the amount of Cu at the same amount of H_3BTC is equivalent with changing the molar ratio of Cu to H_3BTC. This procedure is similar as that used for the attempted incorporation of Mg into Cu–BTC but without addition of magnesium nitrate hexahydrate. Specifically, copper nitrate trihydrate (80%, 60% and 40% of 0.875 g) was dissolved in water (12 mL) and 1,3,5-tricarboxybenzene was dissolved in ethanol (12 mL). Next, the aqueous solution was added to ethanol solution. After stirring for 20 min, the reaction mixture was transferred into autoclave and kept at 120 °C for 12 h. The resulting blue powder was obtained by centrifugation of the final reaction mixture, which was further dried at 120 °C under vacuum for 20 hours. When the mass of copper nitrate trihydrate was 80%, 60% and 40% of 0.875 g, the product was labelled as Cu–BTC (80%), Cu–BTC (60%), and Cu–BTC (40%), respectively.

Characterization methods

Powder X-ray diffraction (XRD) data of various nanomaterials (Cu–BTC, Cu–BTC (80%), Cu–BTC (60%), and Cu–BTC (40%)) were obtained on a Bruker D8 Advance X-ray diffractometer using Cu Kα radiation (0.154 nm) with scanning from 5.00° to 40.00° (2θ) (parameters: voltage (40 kV), current (35 mA), step size (0.020°), and 0.8° min^{-1}). Powder X-ray diffraction measurements (XRD) obtained for the Cu–BTC samples (Mg 20%-Cu–BTC, Mg 40%-Cu–BTC and Mg 60%-Cu–BTC) prepared in the presence of Mg salt were performed on Geigerflex (Rigaku, Inc.) diffractometer using Cu Kα radiation (0.154 nm) from 5.00° to 40.00° (2θ) (parameters: voltage (45 kV), current (35 mA), step size (0.020°), and 1.2° min^{-1}). A Hitachi S-2600 N scanning electron microscope was utilized to obtain the scanning electron microscopy (SEM) images and energy dispersive spectra (EDS). SEM and EDS analyses were performed on a sample powder previously dried and the sample surface was gold metallized.

A Q500 Thermogravimetric analyzer was used for the thermogravimetric analysis (TGA). All TGA data were collected with heating up to 800 °C (heating rate: 10 °C min^{-1}) in flowing air. The nitrogen sorption was performed using ASAP 2010/2020 volumetric adsorption analyzers (Micromeritics Inc.) and ultrahigh-pure nitrogen at −196 °C. Carbon dioxide adsorption at 0 °C and 25 °C for these samples was recorded on an ASAP 2020 volumetric adsorption analyzer. All samples were degassed under vacuum at 200 °C for 2 h before measurements. The specific Brunauer–Emmett–Teller (BET) surface area for all samples were evaluated from N_2 adsorption isotherms in the pressure range of 0.05–0.20. The total pore volumes (V_{total}) for the MOF studied were determined based on the N_2 amount adsorbed at $P/P_0 = 0.99$. Pore size distribution (PSD) of microporous MOFs was obtained using a 2D-nonlocal density functional theory (2D-NLDFT) method for heterogeneous surfaces with SAIEUS program provided by Micromeritics.[29] The micropore volume (V_{micro}) for the MOFs studied were calculated from the cumulative pore volume curve obtained by the 2D-NLDFT method up to pore width of 2 nm. The CO_2/N_2 selectivity was determined by the ideal adsorbed solution theory (IAST) model,[44] based on the equation of $S = n(CO_2)p(N_2)/[n(N_2)p(CO_2)]$ (S: the selectivity for CO_2/N_2; $n(CO_2)$: the CO_2 adsorption amount at $p(CO_2) = 0.15$ bar; $n(N_2)$: the N_2 adsorption amount at $p(N_2) = 0.85$ bar).

Conflicts of interest

There are no financial conflicts to declare.

Acknowledgements

We would like to thank Drs Min Gao and Lu Zou for their technical assistance with the SEM and EDS spectroscopy at the Liquid Crystal Institute, Kent State University.

Notes and references

1 S. Choi, J. H. Drese and C. W. Jones, *ChemSusChem*, 2009, **2**, 796–854.
2 S. Chu, *Science*, 2009, **325**, 1599.
3 X. Zhu, C. Tian, S. M. Mahurin, S.-H. Chai, C. Wang, S. Brown, G. M. Veith, H. Luo, H. Liu and S. Dai, *J. Am. Chem. Soc.*, 2012, **134**, 10478–10484.
4 A. Policicchio, Y. Zhao, Q. Zhong, R. G. Agostino and T. J. Bandosz, *ACS Appl. Mater. Interfaces*, 2014, **6**, 101–108.
5 M. J. Tuinier, M. van Sint Annaland, G. J. Kramer and J. A. M. Kuipers, *Chem. Eng. Sci.*, 2010, **65**, 114–119.
6 D. M. D'Alessandro, B. Smit and J. R. Long, *Angew. Chem., Int. Ed.*, 2010, **49**, 6058–6082.
7 J.-R. Li, R. J. Kuppler and H.-C. Zhou, *Chem. Soc. Rev.*, 2009, **38**, 1477–1504.
8 Y. Yue, P. F. Fulvio and S. Dai, *Acc. Chem. Res.*, 2015, **48**, 3044–3052.
9 K. Leus, Y.-Y. Liu and P. Van Der Voort, *Catal. Rev.*, 2014, **56**, 1–56.
10 D. J. Tranchemontagne, J. L. Mendoza-Cortes, M. O'Keeffe and O. M. Yaghi, *Chem. Soc. Rev.*, 2009, **38**, 1257–1283.
11 K. K. Tanabe and S. M. Cohen, *Chem. Soc. Rev.*, 2011, **40**, 498–519.
12 J. Lee, J. Li and J. Jagiello, *J. Solid State Chem.*, 2005, **178**, 2527–2532.
13 H. Furukawa, K. E. Cordova, M. O'Keeffe and O. M. Yaghi, *Science*, 2013, **341**, 1230444.
14 S. S.-Y. Chui, S. M.-F. Lo, J. P. H. Charmant, A. G. Orpen and I. D. Williams, *Science*, 1999, **283**, 1148–1150.
15 T. Tian, Z. Zeng, D. Vulpe, M. E. Casco, G. Divitini, P. A. Midgley, J. Silvestre-Albero, J.-C. Tan, P. Z. Moghadam and D. Fairen-Jimenez, *Nat. Mater.*, 2017, **17**, 174.
16 C. Zhu, Z. Zhang, B. Wang, Y. Chen, H. Wang, X. Chen, H. Zhang, N. Sun, W. Wei and Y. Sun, *Microporous Mesoporous Mater.*, 2016, **226**, 476–481.
17 X. Mu, Y. Chen, E. Lester and T. Wu, *Microporous Mesoporous Mater.*, 2018, **270**, 249–257.
18 B. Zheng, J. Bai, J. Duan, L. Wojtas and M. J. Zaworotko, *J. Am. Chem. Soc.*, 2011, **133**, 748–751.
19 Y. Cao, Y. Zhao, F. Song and Q. Zhong, *J. Energy Chem.*, 2014, **23**, 468–474.
20 Y. Yang, P. Shukla, S. Wang, V. Rudolph, X.-M. Chen and Z. Zhu, *RSC Adv.*, 2013, **3**, 17065–17072.
21 Y. Zhao, M. Seredych, J. Jagiello, Q. Zhong and T. J. Bandosz, *Chem. Eng. J.*, 2014, **239**, 399–407.
22 B. Szczęśniak, J. Choma and M. Jaroniec, *J. Colloid Interface Sci.*, 2018, **514**, 801–813.
23 K. Schlichte, T. Kratzke and S. Kaskel, *Microporous Mesoporous Mater.*, 2004, **73**, 81–88.
24 C. Gunathilake and M. Jaroniec, *J. Mater. Chem. A*, 2016, **4**, 10914–10924.
25 Z. Bao, L. Yu, Q. Ren, X. Lu and S. Deng, *J. Colloid Interface Sci.*, 2011, **353**, 549–556.
26 X. Kong, E. Scott, W. Ding, J. A. Mason, J. R. Long and J. A. Reimer, *J. Am. Chem. Soc.*, 2012, **134**, 14341–14344.
27 Z.-Y. Yao, J.-H. Guo, P. Wang, Y. Liu, F. Guo and W.-Y. Sun, *Mater. Lett.*, 2018, **223**, 174–177.
28 T. Wang, X. Li, W. Dai, Y. Fang and H. Huang, *J. Mater. Chem. A*, 2015, **3**, 21044–21050.
29 J. Jagiello and J. P. Olivier, *Carbon*, 2013, **55**, 70–80.
30 J. Jagiello, C. Ania, J. B. Parra and C. Cook, *Carbon*, 2015, **91**, 330–337.
31 Q. Y. Yang, C. Y. Xue, C. L. Zhong and J. F. Chen, *AIChE J.*, 2007, **53**, 2832–2840.
32 J. Ludwinowicz and M. Jaroniec, *Carbon*, 2015, **82**, 297–303.
33 W. Huang, X. Zhou, Q. Xia, J. Peng, H. Wang and Z. Li, *Ind. Eng. Chem. Res.*, 2014, **53**, 11176–11184.
34 X. Yan, S. Komarneni, Z. Zhang and Z. Yan, *Microporous Mesoporous Mater.*, 2014, **183**, 69–73.
35 C. Zhu, Z. Zhang, B. Wang, Y. Chen, H. Wang, X. Chen, H. Zhang, N. Sun, W. Wei and Y. Sun, *Microporous Mesoporous Mater.*, 2016, **226**, 476–481.
36 C. Chen, B. Li, L. Zhou, Z. Xia, N. Feng, J. Ding, L. Wang, H. Wan and G. Guan, *ACS Appl. Mater. Interfaces*, 2017, **9**, 23060–23071.
37 X. Mu, Y. Chen, E. Lester and T. Wu, *Microporous Mesoporous Mater.*, 2018, **270**, 249–257.
38 J. Canivet, M. Vandichel and D. Farrusseng, *Dalton Trans.*, 2016, **45**, 4090–4099.
39 D. S. Sholl and R. P. Lively, *J. Phys. Chem. Lett.*, 2015, **6**, 3437–3444.
40 A. W. Thornton, R. Babarao, A. Jain, F. Trousselet and F. X. Coudert, *Dalton Trans.*, 2016, **45**, 4352–4359.
41 S. Chaemchuen, Z. Luo, K. Zhou, B. Mousavi, S. Phatanasri, M. Jaroniec and F. Verpoort, *J. Catal.*, 2017, **354**, 84–91.
42 O. Karagiaridi, N. A. Vermeulen, R. C. Klet, T. C. Wang, P. Z. Moghadam, S. S. Al-Juaid, J. F. Stoddart, J. T. Hupp and O. K. Farha, *Inorg. Chem.*, 2015, **54**, 1785–1790.
43 E. López-Maya, C. Montoro, V. Colombo, E. Barea and J. A. R. Navarro, *Adv. Funct. Mater.*, 2014, **24**, 6130–6135.
44 A. L. Myers and J. M. Prausnitz, *AIChE J.*, 1965, **11**, 121–127.

